Fatigue and Fracture Behavior of Bulk Metallic Glass

Z.F. ZHANG, J. ECKERT, and L. SCHULTZ

Tensile, compressive, cyclic tension-tension, and cyclic compression-compression tests at room temperature were systematically applied to a $Zr_{52.5}Cu_{17.9}Al_{10}Ni_{14.6}Ti_5$ bulk metallic glass for comprehensive understanding of its damage and fracture mechanisms. Under tensile loading, the metallic glass only displays elastic deformation followed by brittle shear fracture. Under compressive loading, after elastic deformation, obvious plasticity (0.5 to 0.8 pct) can be observed before the final shear fracture. The fracture strength under compression is slightly higher than that under tension. The shear fracture under compression and tension does not occur along the maximum shear stress plane. This indicates that the fracture behavior of the metallic glass does not follow the Tresca criterion. The fracture surfaces show remarkably different features, *i.e*., a uniform vein structure (compressive fracture) and round cores coexisting with the radiating veins (tensile fracture). Under cyclic tension-tension loading, fatigue cracks are first initiated along localized shear bands on the specimen surface, then propagated along a plane basically perpendicular to the stress axis. A surface damage layer exists under cyclic compression-compression loading. However, the final failure also exhibits a pure shear fracture feature as under uniaxial compression. The cyclic compression-compression fatigue life of the metallic glass is about a factor of 10 higher than the cyclic tension-tension fatigue life at the same stress ratio. Based on these results, the damage and fracture mechanisms of the metallic glass induced by uniaxial and cyclic loading are elucidated.

I. INTRODUCTION

FROM the 1970s until now, the deformation and fracture mechanisms of amorphous alloys were widely investigated.[1–7] Spaepen[7] established an empirical deformation map and two typical deformation modes, *i.e*., homogenous and inhomogeneous flow at low and high temperatures or low and high strain rates, respectively. The fracture of metallic glasses at low temperatures often occurs in a shear mode and a vein structure was widely observed on the fracture surface.[4,5,6] In the past decade, several families of alloys based on Zr-, Pd-, La-, *etc*. with good glass-forming ability were discovered, and bulk metallic glasses (BMGs) have received much attention.[8,9] Their high strength, high fracture toughness, high hardness, and good corrosion resistance make BMGs attractive candidates for potential industrial applications. Recently, it was found that the compressive fracture plasticity can be significantly improved by different approaches, such as precipitation of nanoscale particles by partial crystallization[10,11] or homogenous dispersion of insoluble particles, or strong fibers as reinforcements.[12–16] Another recently developed technique is to *in-situ* precipitate dendritic crystals, which results in ductile BMG composites.[17–20] However, under tensile loading, nearly all BMGs display zero plasticity even though the compressive fracture plasticity is quite high (>10 pct). This demonstrates that the loading mode strongly affects the mechanical properties of such materials. Therefore, it is necessary to further reveal the effect of various loading modes on the deformation and fracture mechanisms of BMGs.

Z.F. ZHANG, Professor, is with the Shenyang National Laboratory for Materials Science, Institute of Metal Research, Chinese Academy of Sciences, 110016 Shenyang, People's Republic of China. Contact e-mail: zhfzhang@imr.ac.cn J. ECKERT, Professor, is with the Department of Materials and Earth Sciences, Physical Metallurgy Division, Darmstadt University of Technology, D-64287 Darmstadt, Germany. L. SCHULTZ, Professor, is with the Institute of Metallic Materials, D-01171 Dresden, Germany.

Manuscript submitted April 3, 2004.

In order to investigate the mechanical properties and the fracture mechanisms of BMGs, compressive deformation tests are most widely employed. However, tensile and fatigue tests have received less attention and the corresponding fracture mechanisms are poorly understood.[21–30] An open question is whether there is a difference in the fracture mechanisms under compression and tension, because BMGs often display poor plasticity under tensile loading even though they possess very good compressive plasticity.[12,13,16–19] Another question is what leads to the fatigue damage of BMGs since the applied cyclic stress is always far below their yield strength (~1.5 to 2.0 GPa) during fatigue. As is well known, fatigue cracks can nucleate along persistent slip bands (PSBs)[31,32] or deformation bands (DBs)[33,34] in fatigued single crystals. In bicrystals and polycrystals, grain boundaries (GBs) are always potential sites to initiate fatigue cracks due to the impingement of slip bands on the GBs.[35,36] However, there are neither slip systems nor grain boundaries in amorphous alloys. Hence, it is interesting to know more about the origin of fatigue damage during cyclic deformation. In particular, whether fatigue crack can originate from the shear bands in metallic glasses fatigued at low cyclic stress levels. Recently, the fatigue behavior of several metallic glasses was investigated.[22–24,28,30] However, the basic fatigue damage mechanisms were not well clarified in those experiments. Accordingly, the difference in the fatigue cracking mechanisms between metallic polycrystals and amorphous materials is not clear. In the present work, we attempt to systematically elucidate the fundamental damage and fracture mechanisms of a $Zr_{52.5}Cu_{17.9}Al_{10}Ni_{14.6}Ti_5$ bulk metallic glass under tensile, compressive, cyclic tension-tension, and cyclic compression-compression loading.

II. EXPERIMENTAL PROCEDURE

Master ingots with composition $Zr_{52.5}Cu_{17.9}Al_{10}Ni_{14.6}Ti_5$ were prepared by arc melting elemental Zr, Cu, Al, Ni, and Ti with a purity of 99.9 pct in a Ti-gettered argon atmosphere.

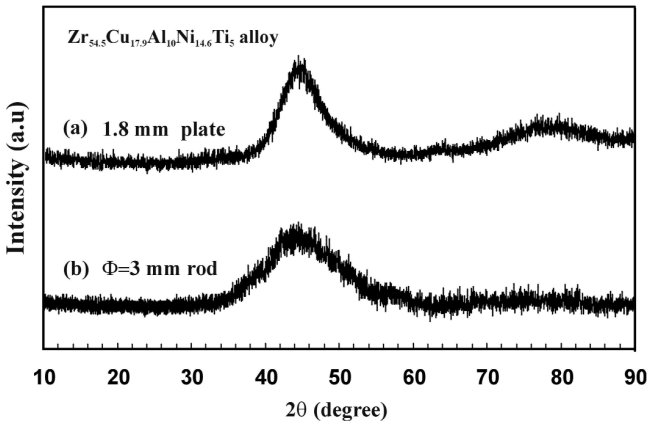

Fig. 1—X-ray diffraction patterns of $Zr_{52.5}Cu_{17.9}Al_{10}Ni_{14.6}Ti_5$ bulk metallic glassy samples for (*a*) tensile and (*b*) compressive tests.

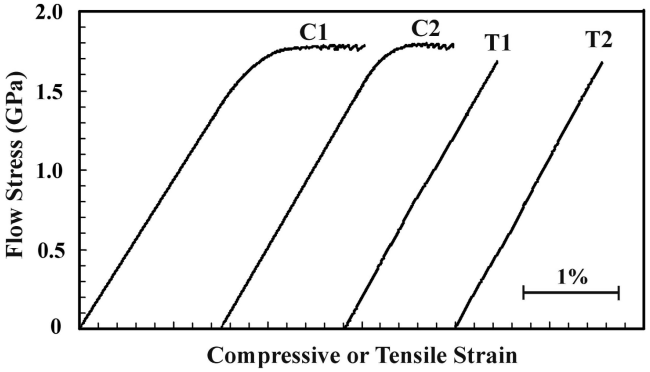

Fig. 2—Stress-strain curves for $Zr_{52.5}Cu_{17.9}Al_{10}Ni_{14.6}Ti_5$ metallic glassy specimens at different strain rates. Compressive tests were performed at strain rates of 10^{-3}/s (C1) and 10^{-4}/s (C2), and tensile tests were done at strain rates of 3×10^{-3}/s (T1) and 3×10^{-4}/s (T2).

The master ingots were remelted several times to achieve homogeneity, followed by casting into two types of copper molds with cavities of $40 \times 30 \times 1.8$ mm or o.d. 3×100 mm. The as-cast samples were analyzed by standard X-ray diffraction (PHILIPS* PW1050 diffractometer using Co K_α radiation) to identify the amorphous structure, as shown in Figure 1. Both the (a) platelike and (b) rodlike samples show only broad diffraction maxima, as is typical for amorphous material. Tensile and cyclic tension-tension specimens with a total length of 40 mm were cut from the plates and were mechanically polished to produce a mirror surface. The gage dimensions were $6 \times 3 \times 1.5$ mm. The o.d. 3-mm rods were cut into 6-mm-high specimens for compressive and cyclic compression-compression tests. The tensile and compressive tests were conducted at different strain rates (10^{-3} to 10^{-4}/s) with an Instron 4652 testing machine at room temperature. The cyclic tension-tension and compression-compression tests were done under stress control. The ratio of the maximum applied stress σ_{max} to the tensile or compressive fracture strength (σ_F^T or σ_F^C) was controlled in the range of 0.5 to 0.8 (cyclic tension-tension) or 0.73 to 0.86 (cyclic compression-compression) at a constant stress ratio $R = \sigma_{min}/\sigma_{max} = 0.1$. A triangle wave with a frequency of 1 Hz was employed for all the fatigue tests. After uniaxial or fatigue fracture, the specimens were investigated with a JEOL† JSM-6400 scanning electron microscope (SEM) and an optical microscope to reveal the fracture surface morphology and the fracture processes.

*PHILIPS is a trademark of Philips Electronic Instruments, Mahwah, NJ.

†JEOL is a trademark of Japan Electron Optics Ltd., Tokyo.

III. EXPERIMENTAL RESULTS

A. *Mechanical Properties*

1. *Tensile and compressive stress-strain curves*

Figure 2 shows the stress-strain curves of the specimens at different strain rates under compressive and tensile loading. For better visibility, the curves are shifted along the strain axis. Under compressive loading, the specimens (C1 and C2) display obvious plasticity (0.5 to 0.8 pct) before failure. Young's modulus is 97.8 ± 5.2 GPa, and the elastic strain is about 1.8 pct. The total strain before failure is 2.5 to 3.0 pct, and the compressive fracture stress σ_F^C is 1.76 ± 0.02 GPa. However, under tensile loading, the specimens (T1 and T2) exhibit only elastic deformation behavior with an elastic strain of ~1.7 pct and subsequent catastrophic fracture without obvious plastic deformation. The fracture strength σ_F^T (=1.66 ± 0.01 GPa) under tension is slightly lower than under compression ($\sigma_F^C = 1.76$ GPa). These results agree well with the literature data reported for Zr-Cu-Al-Ni-Ti glasses.[10,14,37–40] Table I reveals that the compression fracture strength of metallic glasses is often slightly higher than the tensile fracture strength.[2,14–16,37–43] For fully amorphous alloys, the difference between compression and tension seems to be negligible. However, for glassy composites containing hard particles or strong fibers,[15,16] the tension fracture strength σ_F^T is significantly lower than the compression fracture strength σ_F^C. There is only one exception in Table I. For $Zr_{62}Ti_{10}Ni_{10}Cu_{14.5}Be_{3.5}$, metallic glass,[43] the average fracture strength in tension is slightly higher than for compression under a hydrostatic pressure. However, in a more recent report,[25] the tensile fracture stress (1.98 GPa) is quite similar to the compressive fracture strength (2.00 GPa).

2. *Fatigue life curves*

Figure 3(a) shows the fatigue life curves of the present alloy together with data for $Zr_{55}Cu_{30}Al_{10}Ni_5$[29] and $Zr_{59}Cu_{20}Al_{10}Ni_8Ti_3$[44] metallic glasses subjected to cyclic tension-tension loading. At the same, the σ_{max}/σ_F^C ratio, the average fatigue life N_f of the present alloy, is nearly the same as that of $Zr_{59}Cu_{20}Al_{10}Ni_8Ti_3$ metallic glass at the same ratio $R = 0.1$, but obviously lower than that of $Zr_{55}Cu_{30}Al_{10}Ni_5$ metallic glass at the stress ratio $R = 0.5$. One of the reasons for this difference can be attributed to the different stress ratios R. At $R = 0.1$, the cyclic stress amplitude $\sigma_a = (\sigma_{max} - \sigma_{min})/2$ is obviously higher than for $R = 0.5$ with the same σ_{max}/σ_F^C. When the relationship of fatigue life N_f *vs* σ_a/σ_F^C is plotted in Figure 3(b), $Zr_{55}Cu_{30}Al_{10}Ni_5$ always has a relatively lower fatigue life than $Zr_{52.5}Cu_{17.9}Al_{10}Ni_{14.6}Ti_5$ and $Zr_{59}Cu_{20}Al_{10}Ni_8Ti_3$ at the same σ_a/σ_F^C ratio. This indicates that both the stress amplitude σ_a, and the stress ratio R affect the cyclic tension-tension fatigue life of metallic glasses.

Table I. Comparison of the Fracture Strength under Tension and Compression for Different Metallic Glasses

Investigators	Compositions		σ_F^C (GPa)	σ_F^T (GPa)
Conner *et al.*[14]	$Zr_{57}Cu_{15.4}Al_{10}Nb_5Ni_{7.6}$		1.80	1.20
Davis and Kavesh[41]	$Pd_{77.5}Cu_6Si_{16.5}$		1.57	1.44
Donovan[2]	$Pd_{40}Ni_{40}P_{20}$		1.78	1.46
He *et al.*[38]	$Zr_{52.5}Ni_{14.6}Al_{10}Cu_{17.9}Ti_5$		1.82	1.66
Inoue *et al.*[42]	$Cu_{60}Zr_{30}Ti_{10}$		2.15	2.00
Liu *et al.*[37]	$Zr_{52.5}Ni_{14.6}Al_{10}Cu_{17.9}Ti_5$		1.72	1.65
Lewandowski and	$Zr_{40}Ti_{12}Ni_{9.4}Cu_{12.2}Be_{26.4}$		2.01*	1.92*
Lowhaphandu.[25]			2.00	1.98
Lowhaphandu *et al.*[43]	$Zr_{62}Ti_{10}Ni_{10}Cu_{14.5}Be_{3.5}$		1.91*	1.98*
Zhang *et al.*[39]	$Zr_{59}Cu_{20}Al_{10}Ni_8Ti_3$		1.69	1.58
Hirano *et al.*[15]	$Zr_{55}Cu_{30}Ni_5Al_{10}$		1.82	~1.51
		+5 pct ZrC	1.93	—
		+7.5 pct ZrC	2.00	~1.51
		+10 pct ZrC	2.06	—
		+12.5 pct ZrC	2.14	—
		+15 pct ZrC	2.26	~1.51
Qiu *et al.*[16]	$(Zr_{55}Cu_{30}Ni_5Al_{10})_9$	+10 pct W	~1.75	~1.00
		+20 pct W	~1.90	~1.23
	$_{8.5}Si_{1.5}$	+40 pct W	~1.96	~1.36
		+60 pct W	~2.04	~1.43
		+70 pct W	~2.06	~1.05
Present result	$Zr_{52.5}Cu_{17.9}Al_{10}Ni_{14.6}Ti_5$		1.76	1.66

*The mechanical tests were conducted under hydrostatic pressure.
Note: σ_F^C is compression fracture strength, and σ_F^T is tensile fracture strength.

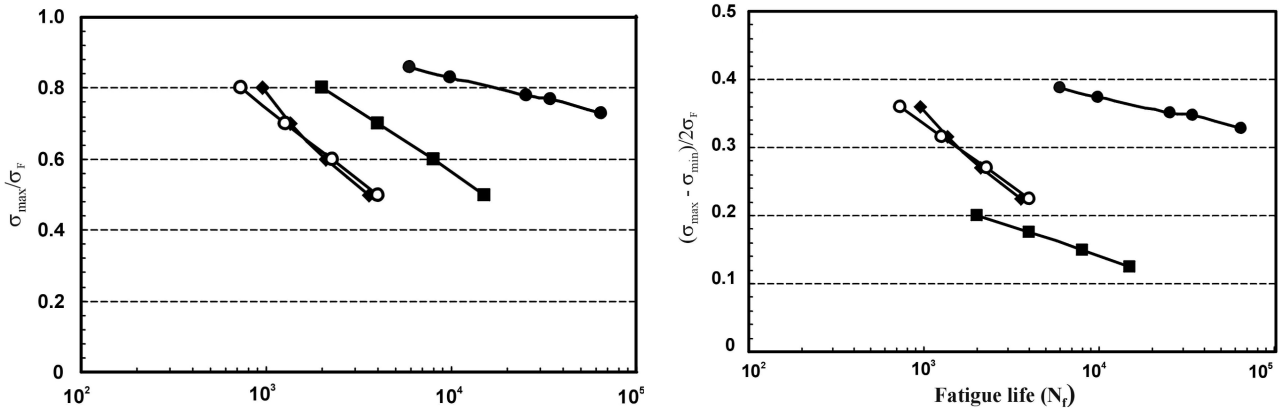

(*a*)

On the other hand, the cyclic compression-compression fatigue life of $Zr_{52.5}Cu_{17.9}Al_{10}Ni_{14.6}Ti_5$ metallic glass is about a factor of 10 higher than the cyclic tension-tension fatigue life, as shown in Figures 3(a) and (b). This demonstrates that the loading mode plays an important role in the fatigue life of metallic glasses due to the difference in the fatigue damage mechanisms. The stress-strain curves in Figure 2 reveal that the applied maximum cyclic stresses, σ_{max}, are in the elastic deformation regime for all the metallic glasses. For crystalline materials, it is well known that there is no fatigue damage when the deformation is purely elastic.[45] However, at $\sigma_{max}/\sigma_F^T = 0.5$ to 0.8 or $\sigma_{max}/\sigma_F^C = 0.73$ to 0.86, the fatigue lives of all the metallic glasses are only in the range of 10^3 to 10^5, which is typical for low-cycle-fatigue failure.

B. *Fracture Surface Observations*

1. *Compressive fracture features*

The SEM observations show that the fracture under compression always occurs in a shear mode (Figure 4(a)). The compressive fracture surface makes an angle θ_C with the stress axis and can be directly measured. For the present specimens, the compressive fracture angle θ_C between the

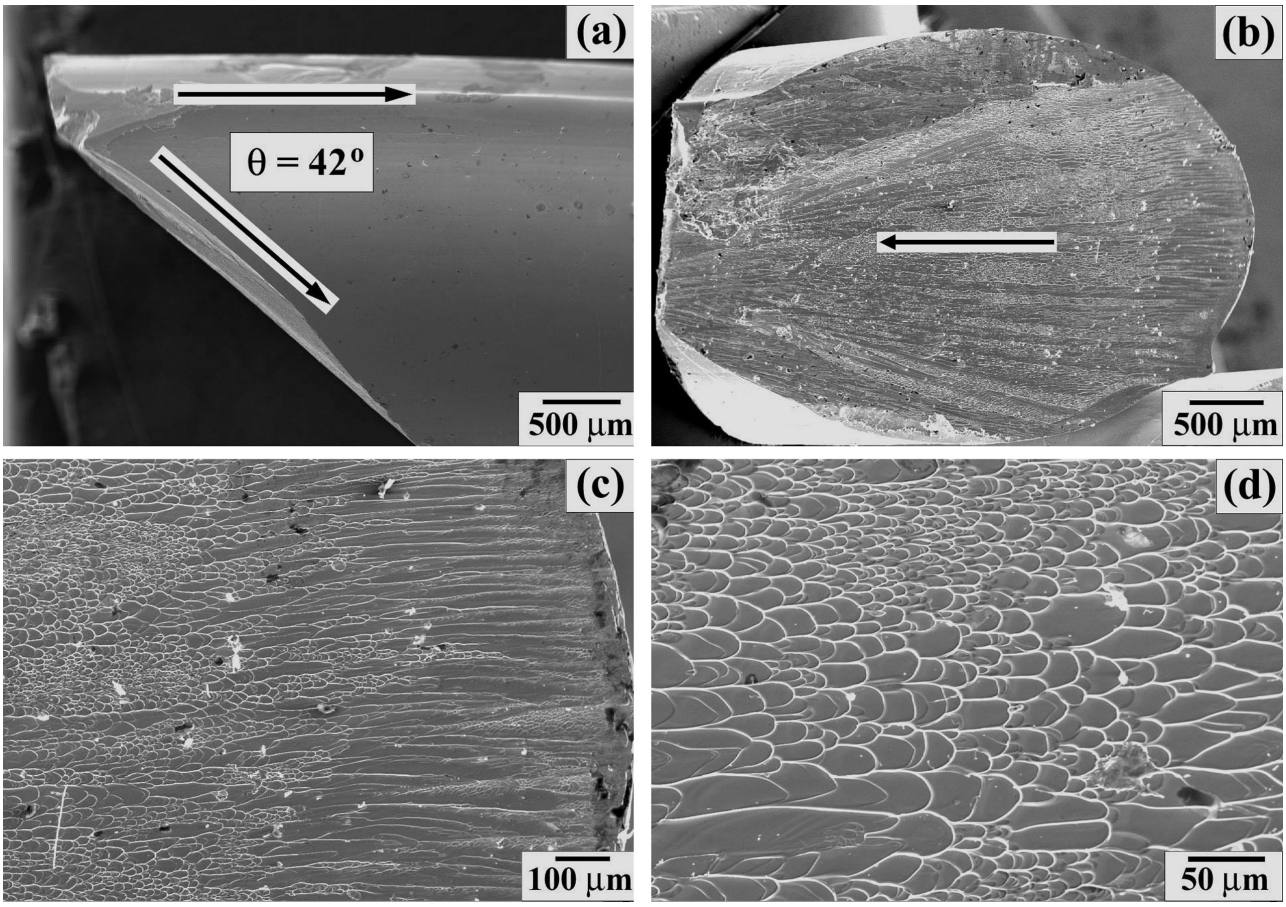

Fig. 4—Compressive fracture surface features of $Zr_{52.5}Cu_{17.9}Al_{10}Ni_{14.6}Ti_5$ metallic glassy specimens: (*a*) the fracture surface makes an angle of 42 deg with respect to the loading axis; (*b*) overall fracture surface; and (*c*) and (*d*) typical vein structure, showing a pure shear fracture process.

stress axis and the fracture surface is 42 deg. The fracture surface is relatively flat on a macroscopic scale and displays a typical shear fracture feature (Figure 4(b)). This fracture behavior has been widely observed for many other metallic glasses.[4–6,10,25,37–40,43,46] Since metallic glasses have an isotropic structure, their fracture angle plane should be along the maximum shear stress plane, *i.e.*, $\theta_C = 45$ deg, in terms of the Tresca criterion.[2] However, careful measurements by some investigators showed that θ_C is approximately 41 to 43 deg, *i.e.*, smaller than 45 deg. A comparison of literature data is given in Table II.[2,4–6,10,25,38–40,43,46] In most cases, the compressive fracture of metallic glasses does not exactly occur along the maximum shear stress plane and, accordingly, does not follow the Tresca criterion.

Further observations show that the typical feature on the fracture surfaces is a veinlike structure (Figures 4(c) and (d)). This veinlike structure often spreads over the entire fracture surface and extends along a uniform direction, as marked by the arrow in Figure 4(b). The uniform arrangement of the veins exactly corresponds to the propagation direction of the shear band, which is confirmed by Figures 4(a) through (d). The veinlike structure was attributed to local melting within the shear band induced by the high elastic energy release upon instantaneous fracture.[37,46] The molten material easily flows and creates a veinlike structure feature. As a result, the compressive fracture surfaces of different glasses show almost the same veinlike structure, clearly demonstrating a pure shear fracture process.

Table II. Comparison of the Compressive Shear Fracture Angle θ_C for Different Metallic Glasses

Investigators	Compositions	Fracture Angle (θ_C)
Donovan[2]	$Pd_{40}Ni_{40}P_{20}$	41.9 ± 1.2 deg
He *et al.*[38]	$Zr_{52.5}Ni_{14.6}Al_{10}Cu_{17.9}Ti_5$	40 to 45 deg
Lewandowski and Lowhaphandu[25]	$Zr_{40}Ti_{12}Ni_{9.4}Cu_{12.2}Be_{26.4}$	40.4 ± 1 deg
Lowhaphandu *et al.*[43]	$Zr_{62}Ti_{10}Ni_{10}Cu_{14.5}Be_{3.5}$	41.6 ± 2.1 deg
Wright *et al.*[46]	$Zr_{40}Ti_{14}Ni_{10}Cu_{12}Be_{24}$	42 deg
Zhang *et al.*[39]	$Zr_{59}Cu_{20}Al_{10}Ni_8Ti_3$	43 deg
Present result	$Zr_{52.5}Cu_{17.9}Al_{10}Ni_{14.6}Ti_5$	42 deg

2. *Tensile fracture features*

For the specimens under tension, shear fracture is still the unique failure mode (Figure 5(a)). The formation and propagation of one major shear band dominates the fracture process. However, for the present specimens, the tensile fracture angle θ_T between the tensile axis and the fracture plane is 56 deg, which significantly deviates from the maximum shear stress plane. This result is consistent with previous observations on the same metallic glass under tensile deformation.[37,38]

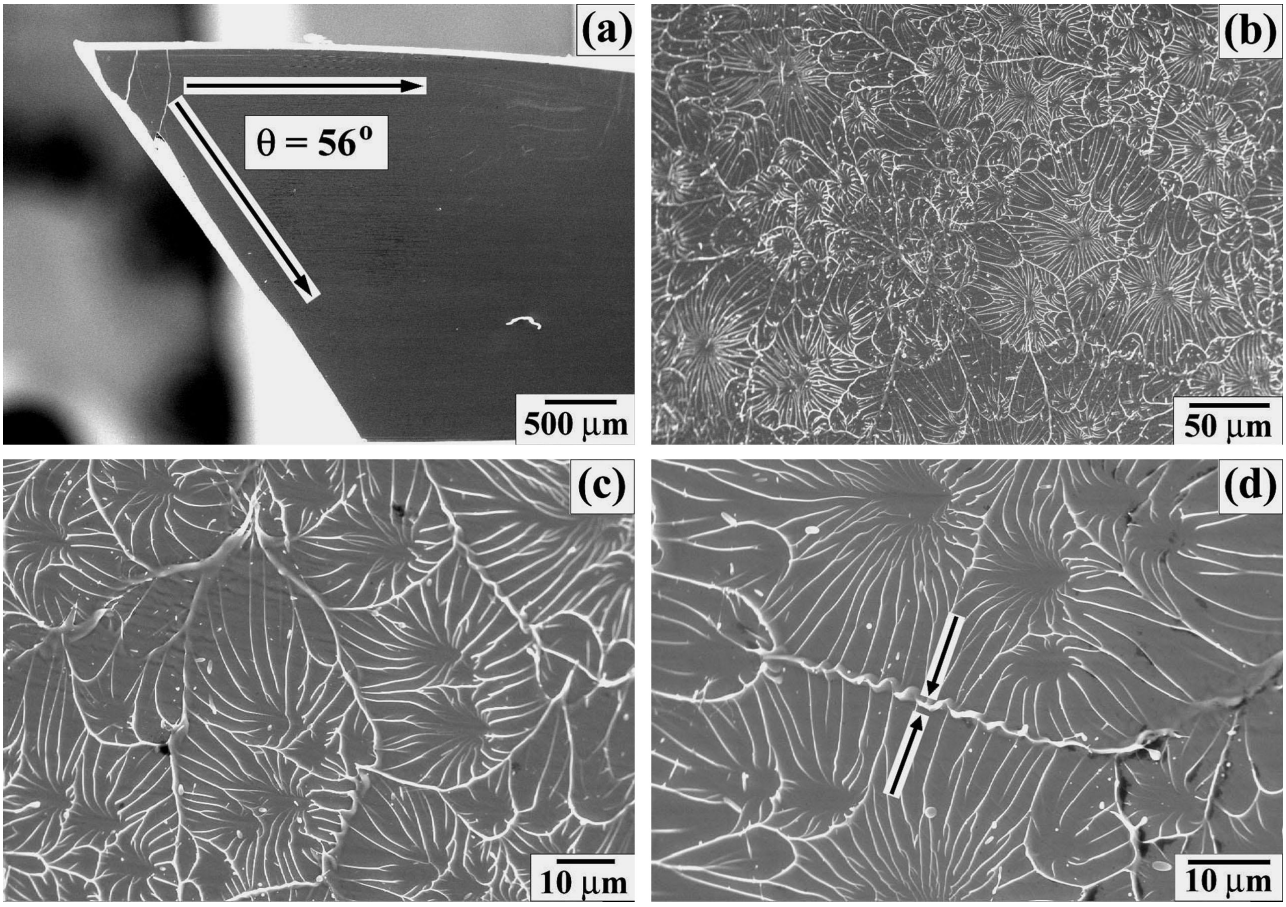

Fig. 5—Tensile fracture surface features of $Zr_{52.5}Cu_{17.9}Al_{10}Ni_{14.6}Ti_5$ metallic glassy specimens: (*a*) the fracture surface makes an angle of 56 deg with respect to the loading axis; and (*b*)–(*d*) cores coexisting with radiating veins, showing a combined fracture mode.

Table III. Comparison of the Tensile Shear Fracture Angle θ_T for Different Metallic Glasses

Investigators	Compositions	Fracture Angle (θ_T)
Alpas *et al.*[48]	$Ni_{78}Si_{10}B_{12}$	55 deg
Bengus *et al.*[49]	$Fe_{70}Ni_{10}B_{20}$	60 deg
Davis and Yeow[50]	$Ni_{49}Fe_{29}P_{14}B_6Si_2$	53 deg
He *et al.*[38]	$Zr_{52.5}Ni_{14.6}Al_{10}Cu_{17.9}Ti_5$	55 to 65 deg
Inoue *et al.*[51]	$Zr_{65}Ni_{10}Al_{7.5}Cu_{7.5}Pd_{10}$	50 deg
Inoue *et al.*[42]	$Cu_{60}Zr_{30}Ti_{10}$	54 deg
Liu *et al.*[37]	$Zr_{52.5}Ni_{14.6}Al_{10}Cu_{17.9}Ti_5$	53 to 60 deg
Lewandowski and Lowhaphandu[25]	$Zr_{40}Ti_{12}Ni_{9.4}Cu_{12.2}Be_{26.4}$	55 ± 3.3 deg
Lowhaphandu *et al.*[43]	$Zr_{62}Ti_{10}Ni_{10}Cu_{14.5}Be_{3.5}$	57 ± 3.7 deg
Megusar *et al.*[52]	$Pd_{80}Si_{20}$	50 deg
Mukai *et al.*[53]	$Pd_{40}Ni_{40}P_{20}$	56 deg
Noskova *et al.*[54]	$Co_{70}Si_{15}B_{10}Fe_5$	60 deg
Takayama[55]	$Pd_{77.5}Cu_6Si_{16.5}$	50 to 51 deg
Xiao *et al.*[47]	$Zr_{52.5}Cu_{15}Al_{10}Ni_{10}Be_{12.5}$	55 deg
Zhang *et al.*[39]	$Zr_{59}Cu_{20}Al_{10}Ni_8Ti_3$	54 deg
Present Result	$Zr_{52.5}Ni_{14.6}Al_{10}Cu_{17.9}Ti_5$	56 deg

The deviation of the fracture angle from 45 deg has widely been observed for different metallic glasses. For comparison, a summary of the fracture angles (θ_T) for different glassy alloys is given in Table III. Apparently, the tensile fracture angles θ_T are in the range of 50 to 65 deg; *i.e.*, they are distinctly larger than 45 deg. Therefore, it can be concluded that the deviation of fracture angles (θ_T or θ_C) from 45 deg is a common phenomenon in most metallic glasses both under tension and under compression.

The tensile fracture surfaces exhibit an interesting effect that can be described as many round cores with different diameters, as shown in Figures 5(b) through (d). Recently, the same fracture feature was also observed on the tensile fracture surface of $Cu_{60}Zr_{30}Ti_{10}$, $Zr_{52.5}Cu_{15}Al_{10}Ni_{10}Be_{12.5}$, and $Zr_{59}Cu_{20}Al_{10}Ni_8Ti_3$ metallic glasses.[39,40,42,47] The tensile fracture surfaces demonstrate that the round cores always coexist with a radiating veinlike structure (Figure 5(d)). Two veins from different directions impinge each other to form a clear boundary, as indicated by the arrows. Therefore, the tensile fracture feature is significantly different from the uniform vein structure observed on the compressive fracture surfaces. The two typical fracture features should reflect the difference in the fracture mechanisms of metallic glass under compressive and tensile loading and will be discussed in Section IV–A.

3. *Cyclic tension-tension fracture features*

Figure 6(a) shows the fatigue fracture surface after cyclic tension-tension loading at $\sigma_{max}/\sigma_F = 0.7$. The fracture surface is basically perpendicular to the loading direction rather than inclined to it. Fatigue cracks originate from the surface,

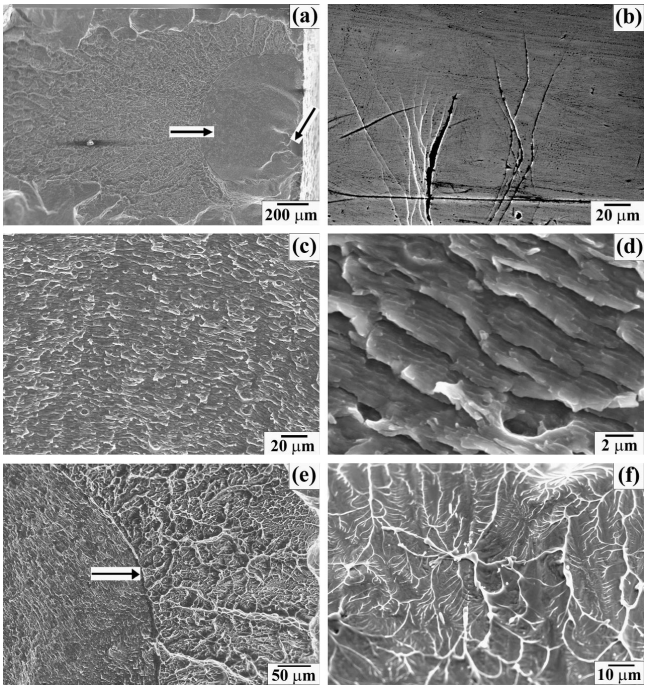

Fig. 6—Cyclic tension-tension damage and fracture surface features of $Zr_{52.5}Cu_{17.9}Al_{10}Ni_{14.6}Ti_5$ metallic glassy specimens: (*a*) overall fatigue fractography; (*b*) surface shear bands and fatigue cracks developed from the shear bands; (*c*) fatigue crack propagation region at low magnification and (*d*) at high magnification; (*e*) boundary between propagation region and final fracture region; and (*f*) fracture feature at the final shear fracture region.

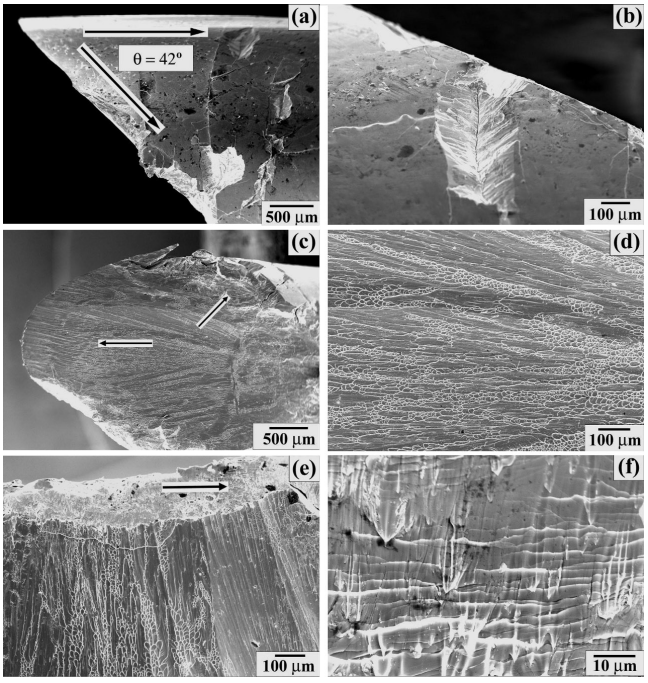

Fig. 7—Cyclic compression-compression damage and fracture surface features of $Zr_{52.5}Cu_{17.9}Al_{10}Ni_{14.6}Ti_5$ metallic glassy specimens: (*a*) the fracture surface makes an angle of 42 deg with respect to the loading axis; (*b*) surface damage and fatigue crack; (*c*) overall fatigue fractography, showing a pure shear fracture feature; (*d*) typical vein structure on the shear fracture surface; and (*e*) and (*f*) fatigue damage within the surface layer of the specimen.

as indicated by the arrows, which is similar to previous observations for fatigued $Fe_{74.5}Cr_{3.5}Si_{10}B_{12}$ and $Zr_{55}Cu_{30}Al_{10}Ni_5$ metallic glasses.[28,29,30] On the surface, there are several cracks (Figure 6(b)). Besides (Figure 6(a)), there is a half-circle region, which corresponds to the initiation of the surface fatigue crack. The fracture feature in the half-circle region is shown in more detail in Figures 6(c) and (d). Many fatigue striations can be clearly seen, indicating a slow propagation of the fatigue crack. There is a clear boundary between the half-circle region and the outside part, as indicated in Figure 6(e). The fatigue fracture surface is similar to the observations for $Zr_{55}Cu_{30}Al_{10}Ni_5$ metallic glass under cyclic tension-tension and cyclic tension-compression loading.[29,30] However, the fracture features in the two regions show no sign of a vein structure as in Figures 4 and 5. This indicates that no melting occurs during the propagation of the fatigue crack. Accordingly, there is a significant difference between the uniaxial tension and cyclic tension-tension fracture mechanisms. Besides the fatigue crack propagation region, the region of the fast final fracture contains the veinlike structure (Figure 6(f)), which is somewhat similar to the tensile fracture feature.

4. *Cyclic compression-compression fracture features*

When the metallic glass is subjected to cyclic compression-compression loading, all specimens fail in a brittle shear mode (Figure 7(a)), analogous to the compressive fracture feature. Another interesting finding is that the fracture angle under cyclic compression-compression loading is still equal to 42 deg, which is identical to the compressive fracture angle θ_C. On the surface of the fatigued specimens, there are many cracks and seriously damaged regions, such as husking of some small metallic glass pieces, as clearly seen in Figure 7(b). The shear band also propagates along a uniform direction, as indicated by the horizontal arrow in Figure 7(c). Moreover, a vein structure can be clearly seen on the fracture surface (Figure 7(d)), which is identical with the compressive fracture feature in Figure 4. Besides the vein structure, there are some strongly damaged regions, namely, a surface damage layer, as indicated by the upward pointing arrow in Figure 7(c). However, under compressive fracture, the specimen surfaces are smooth (Figure 4(a)), indicating an obvious difference in the damage mechanism compared to uniaxial compression. Furthermore, the shear band does not propagate through the entire specimen and often changes its path when approaching the surface damage layer (Figure 7(e)). Within this region, the specimen has undergone serious damage, as shown in Figure 7(f). The surface damage layer often consists of multiple shear bands and small fatigue cracks or husking of small pieces, which were not observed for uniaxially compressed samples. From all these observations, it can be concluded that the fatigue damage and fracture mechanisms of metallic glass under cyclic tension-tension and cyclic compression-compression loading are significantly different. One distinct difference is that there is no propagation of the main fatigue crack during cyclic compression-compression deformation.

IV. DISCUSSION

A. *Tensile and Compressive Fracture Mechanisms*

The resolved shear stress and the normal stress on any shear plane of a specimen under tension or compression are illustrated in Figures 8(a) and (b). According to the Tresca criterion,[2] all the metallic glassy specimens should preferentially shear fracture along the maximum shear stress plane (45 deg) under tension or compression. However, the experimental results described in Section III further prove that the Tresca criterion is invalid for metal glasses for both under compression and tension.[39,40] Normally, the metallic glasses display significantly asymmetric features. First, the fracture strength σ_F^C under compression is slightly higher than that (σ_F^T) under tension for most metallic glasses, as listed in Table I. Second, as shown in Tables II and III,[2,25,37–55] the tensile shear fracture angle θ_T is larger than 45 deg, but the compressive shear fracture angle θ_C is smaller than 45 deg, *i.e.*,

$$0 < \theta_C < 45 \text{ deg} < \theta_T < 90 \text{ deg} \qquad [1]$$

Third, the fracture surface features are also different under the two loading modes, as shown in Figures 4 and 5. For better understanding of such asymmetry in metallic glasses, the Mohr–Coulomb criterion was employed both for compressive and tensile fracture.[39,40] However, sometimes, the fracture of some metallic glasses can occur on the plane perpendicular to the loading direction.[40] Therefore, we should consider the fracture mechanisms of metallic glasses, induced by compression and tension, respectively. As illustrated in Figure 8, the maximum shear stress or normal stress occurs on the plane with respect to 45 or 90 deg. In the case of compression, as shown in Figure 4, the uniform veins on shear fracture surface indicate that the compressive fracture process of a metallic glass is mainly controlled by the resolved shear stress. The shear fracture mechanism has been previously explained by the Mohr–Coulomb criterion.[39,40] Therefore, the shear fracture angle is consistent with the observations for various metallic glasses, as listed in Table II.

However, in the case of tension, as shown in Figure 5, the voidlike vein structure on the tensile fracture surface indicates an apparent different failure feature from compressive failure. Here, we consider that the tensile shear fracture is mainly controlled by normal tensile stress σ_θ, and the shear stress τ_θ only plays an additional role in the fracture process. This is quite different from our recent understanding about tensile shear fracture.[39,40] Therefore, a new concept of effective stress σ_E is proposed for the first time and can be expressed as

$$\sigma_E = \sigma_\theta + \beta \cdot \tau_\theta \geq \sigma_0 \qquad [2]$$

As illustrated in Figures 9(a) and (b), σ_0 is the critical tensile fracture stress on a plane without shear stress, and β is a constant indicating the effect of shear stress on the plane. By substituting $\sigma_\theta = \sigma \sin^2(\theta)$ and $\tau_\theta = \sigma \sin(\theta) \cos(\theta)$ into Eq. [2], we obtain

$$\sigma_E = \sigma \cdot \sin(\theta) \cdot [\sin(\theta) + \beta \cdot \cos(\theta)] \qquad [3]$$

The distribution of the effective stress σ_E and normal tension stress σ_θ on any plane can be seen in Figure 9(c). Obviously, the maximum value of the effective stress σ_E does not occur on the plane of 45 or 90 deg with respect to loading direction. When the effective stress σ_E is equal to or larger than the critical tension fracture stress σ_0, the metallic glass will fracture along the shear plane. The effective stress σ_E will reach its maximum value at point A, B, C, or D under the following condition:

$$\frac{\partial \sigma_E}{\partial \theta} = \sigma \cdot [\sin(2\theta) + \beta \cdot \cos(2\theta)] = 0 \qquad [4]$$

The intersection angle between lines $\overline{OO1}$ and $\overline{OA}$ in Figure 9(c) is the tensile fracture angle θ_T, which is larger than 45 deg. Therefore, the tensile fracture plane is neither

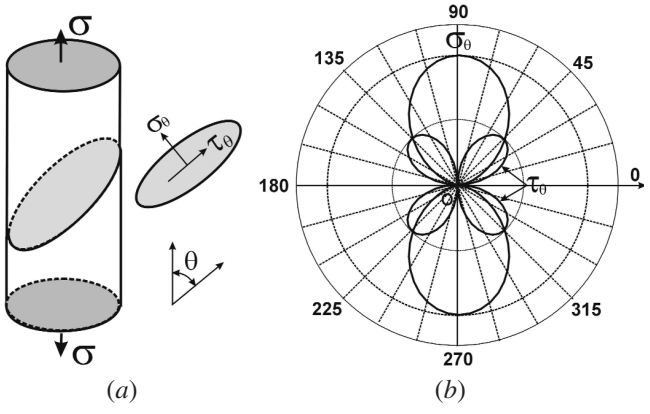

Fig. 8—(*a*) Schematic illustration of the shear plane in the specimen and (*b*) distribution of resolved shear stress and normal stress on any shear plane.

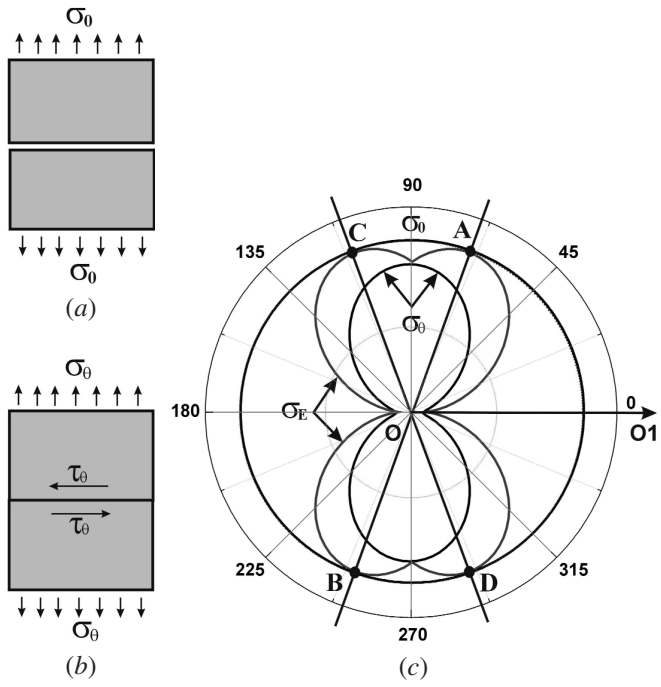

Fig. 9—(*a*) Schematic illustration of normal tensile fracture without shear stress on the fracture plane; (*b*) combined stresses of shear and normal tension stress for a tensile specimen; and (*c*) distribution of the effective stress on any shear plane.

along the maximum shear stress plane nor along the plane perpendicular to the stress axis. In most cases, the fracture angle is in the range of 50 to 65 deg, as listed in Table III. This indicates that the orientations of fracture planes in metallic glasses are strongly affected by the loading mode. In general, the compressive shear failure of metallic glasses is mainly controlled by the shear stress; however, the tensile shear failure is mainly controlled by the normal stress. As a result, the shear failure of metallic glasses often displays an asymmetric feature. On the other hand, the asymmetry of the preceding shear fracture might be associated with the difference in the free volume during compression and tension. This indicates that, in microscale, the different combinations of shear and normal stress strongly affect the distribution of free volume in details, leading to the difference in the coalescence and motion of free volume in the metallic glass. Rearrangement of free volume should somehow contribute to the coalescence of free volume into shear bands and perhaps also to their propagation, furthermore resulting in the asymmetry of shear failure under tension and compression.

B. *Fatigue Fracture Mechanisms*

The facture surface observations under cyclic tension-tension conditions of the present glass are quite similar to our previous results on $Zr_{59}Cu_{20}Al_{10}Ni_8Ti_3$.[44] Normally, the formation of shear bands is critical for the onset of fatigue damage, and cyclic (tension-tension) loading promotes the formation of shear bands. However, the shear bands do not spread over the entire section of the specimen, but only appear at some local sites. This means that there exists a stress concentration on the specimen surface, which can activate the nucleation of shear bands even at a stress level lower than the yield stress. With further cyclic deformation, fatigue cracks often develop from the shear bands, as observed in Figure 6(b). Argon[1] and Spaepen[7] proposed an excess free volume within a narrow shear band due to shear-induced disordering and diffusion-controlled reordering. In general, the free volume region is mechanically weak relative to the surrounding volume, and can be regarded as a potential site for the nucleation of a fatigue crack. Under cyclic tension-tension loading, the gradual weakening, dilation, tearing, and final opening of the shear bands will result in the formation of a fatigue crack, as discussed previously.[44] Along the fatigue crack propagation path, normally, no veinlike structure can be observed in Figures 6(c) and (d), which is different from the findings on the tensile fracture surfaces. This indicates that the propagation of the fatigue crack did not result in melting of the metallic glass because the released elastic energy in the tip of the fatigue crack is too low for local melting.[21] In summary, the cyclic tension-tension damage and fracture mechanisms of metallic glasses include formation of local shear bands at a low stress level, nucleation of fatigue cracks, propagation of the fatigue crack with favorable orientation, and the final fracture.

Under cyclic compression-compression loading, the fatigue fracture behavior of metallic glasses has not been reported previously. It can be concluded that the fatigue damage processes consists of (1) formation of shear bands on the specimen surfaces; (2) initiation of fatigue cracks along the formed shear bands, as observed in Figures 7(a) and (b); (3) husking of small particles; and (4) formation of a surface damage layer, including shear bands, fatigue cracks, and husking of some particles. This fatigue damage mechanism is quite different from the cyclic tension-tension damage mechanism. The main differences include the following: (1) none of the formed fatigue cracks develops into a major crack; (2) the fatigue damage appears mainly in a surface damage layer under cyclic compression-compression loading; and (3) the final failure under cyclic compression-compression occurs along a shear plane, which makes the same angle (42 deg) with the compressive axis as θ_C. Hence, the final fracture behavior is quite similar to the uniaxial compressive fracture of metallic glasses, indicating that the constant α should be invariant for the fracture processes under uniaxial compression and cyclic compression-compression testing. Since the shear bands and fatigue cracks always nucleate on the specimen surface and lead to the formation of a surface damage layer, as shown in Figures 7(a), (b), (c), (e), and (f), the cyclic compression-compression fatigue damage process can be schematically illustrated, as in Figure 10(a). With increasing cycle number, the surface damage layer will gradually propagate toward the interior of the specimen, and, accordingly, the effective area of the specimen will decrease continuously. For a better understanding of the critical fatigue fracture conditions of a metallic glass, the two stress Mohr circles for σ_F^C and $\sigma_{\max}$, and the two critical fracture lines **AB** and **CD**, are schematically illustrated, as in Figure 10(b). Since $\sigma_{\max} = (0.73 \text{ to } 0.86)\,\sigma_F^C$, the initial applied stress cannot lead to shear fracture of the specimen in the beginning of cyclic deformation. With the development of the surface damage layer, the critical compressive fracture line **AB** will drop gradually due to the continuous reduction in the effective area of the specimen. When the critical shear fracture stress τ_0 decreases to τ_0^D, the critical compressive fracture line **AB** will drop to **CD** and touch the Mohr circle of the maximum compressive stress $\sigma_{\max}$. This corresponds to the final shear fracture of the specimen, as illustrated in Figure 10(c). Therefore, the critical cyclic compression-compression fracture condition of metallic glass can be expressed as

$$\tau_\theta \geq \tau_0^D + \alpha \cdot \sigma_\theta \qquad [5]$$

When the maximum compression stress $\sigma_{\max}$ is higher than the critical stress, *i.e.*,

$$\sigma_{\max} \geq \frac{2\tau_0^D}{\sqrt{1 + (\alpha)^2} + \alpha} \qquad [6]$$

the metallic glass will fail in a shear fracture mode upon fatigue fracture, as observed in Figure 7(a) and illustrated in Figure 10(c). It is suggested that the cyclic compression-compression fatigue damage and the fracture of metallic glass are due to the continuous development of the surface damage layer. This layer often consists of multiple shear bands and small cracks or husking of small particles rather than to the propagation of a single fatigue crack, as under cyclic tension-tension loading. Hence, the damage process of a metallic glass under cyclic compression-compression loading can distribute over the entire specimen surface rather than being localized in one single shear band or fatigue crack. This damage feature is more homogenous than that under cyclic tension-tension loading. The development of the surface damage layer rather than the propagation of a

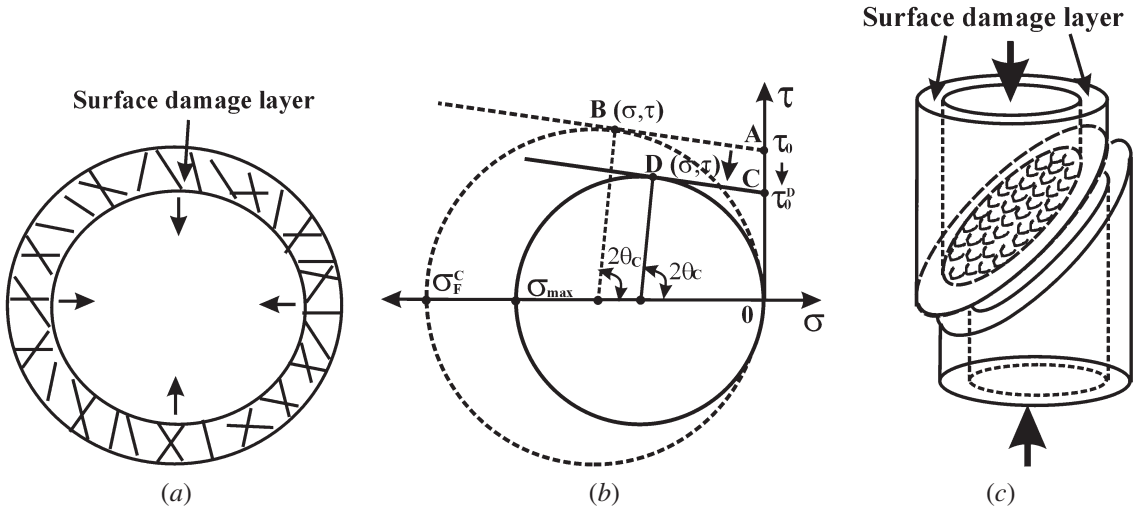

Fig. 10—Schematic illustration of the cyclic compression-compression fracture processes of metallic glass: (*a*) formation and propagation of the surface damage layer; (*b*) critical compressive fracture lines (**AB** and **CD**) and the stress distribution on the two Mohr circles under compressive and cyclic compression-compression loading; and (*c*) final pure shear fracture process across the entire specimen.

single fatigue crack controls the fatigue process. The relatively homogenous distribution of fatigue damage under cyclic compression-compression requires more accumulation of cyclic deformation. As a result, the specimen displays a higher fatigue life than under cyclic tension-tension loading.

V. CONCLUSIONS

1. The fracture behavior of metallic glasses often displays a significant asymmetry. First, the fracture strength under compression is slightly higher than that under tension for most metallic glasses. Second, the compressive and tensile shear fracture angles (θ_C and θ_T) obey the following relation: $0 < \theta_C < 45$ deg $< \theta_T < 90$ deg. Third, the compressive failure always causes relatively uniform veins with the same direction on the fracture surface; however, some round cores with radiating veins appear on the tensile fracture surface. Correspondingly, the fracture mechanisms of metallic glasses should be considered to be induced by compression and tension, respectively. An important fact is that the Tresca criterion is invalid for both compressive and tensile shear fracture of metallic glasses. It is suggested that the compressive and tensile shear failure of metallic glasses is mainly controlled by shear stress and normal stress, respectively.
2. The fatigue damage and fracture mechanisms of metallic glass are also different depending on the cyclic loading mode. Under cyclic tension-tension loading, fatigue cracks first initiate along the shear bands on the surface, then propagate along a plane basically perpendicular to the loading direction. The fracture surface can be divided into two regions, *i.e.*, the propagation region and the final fast fracture region. In the crack propagation region, there are many striation-like bands, which are induced by the gradual propagation of the fatigue crack. No veinlike fracture feature can be observed. Under cyclic compression-compression loading, a surface damage layer forms on the specimen, including shear bands, fatigue cracks, or husking of pieces. None of the fatigue cracks develops into a single crack and the final failure occurs in a shear mode similar to the shear fracture under uniaxial compression. It is suggested that the cyclic compression-compression fatigue damage and fracture of metallic glass is linked with a continuous decrease in the critical shear fracture stress τ_0 due to reduction of the effective area of the specimen. The development of the surface damage layer rather than the propagation of a single fatigue crack controls the fatigue, which results in a higher cyclic compression-compression fatigue life than under cyclic tension-tension loading.

ACKNOWLEDGMENTS

The authors thank H. Grahl, R.-H. Reiter, H. Schulze, and A. Schwab for sample preparation and H.-J. Klauβ for assistance with the mechanical tests. This work was supported by the German Science Foundation (DFG) under Grant No. Ec 111/10-1 and by the EU *via* the RTN-Network on bulk metallic glasses under Contract No. HPRN-CT-2000-00033. One of the authors (ZFZ) acknowledges the Alexander von Humboldt (AvH) Foundation for providing a postdoctoral fellowship, National Natural Science Funds of China (NSFC) and the "Hundred of Talent Project" supported by the Chinese Academy of Sciences.

REFERENCES

1. A.S. Argon: *Acta Metall.*, 1979, vol. 27, p. 47.
2. P.E. Donovan: *Acta Metall.*, 1989, vol. 37, p. 445.
3. R. Huang, Z, Suo, J.H. Prevost, and W.D. Nix *J. Mech. Phys. Solids*, 2002, vol. 50, p. 1011.
4. H.J. Leamy, H.S. Chen, and T.T. Wang: *Metall. Trans.*, 1972, vol. A, pp. 699-708.
5. Y. Leng and T.H. Courtney: *J. Mater. Sci.*, 1991, vol. 26, p. 588.
6. C.A. Pampillo: *J. Mater. Sci.*, 1975, vol. 10, p. 1194.
7. F. Spaepen: *Acta Metall.*, 1977, vol. 25, p. 407.
8. A. Inoue: *Acta Mater.*, 2000, vol. 48, p. 279.
9. W.L. Johnson: *MRS Bull.*, 1999, vol. 24 (10), p. 42.

10. J. Eckert, U. Kühn, N. Mattern, A. Reger-Leonhard, and M. Heilmaier: *Scripta Mater*., 2001, vol. 44, p. 1587.
11. C. Fan and A. Inoue: *Appl. Phys. Lett*., 2000, vol. 77, p. 46.
12. H. Choi-Yim, R. Busch, U. Köster, and W.L. Johnson: *Acta Mater*., 1999, vol. 47, p. 2455.
13. H. Choi-Yim, J, Schroers, and W.L. Johnson: *Appl. Phys. Lett*., 2002, vol. 80, p. 1906.
14. R.D. Conner, H. Choi-Yim, and W.L. Johnson: *J. Mater. Res*., 1999, vol. 14, p. 3292.
15. T. Hirano, H. Kato, A. Matsuo, Y. Kawamura, and A. Inoue: *Mater. Trans., JIM*, 2000, vol. 41, p. 1454.
16. K.Q. Qiu, A.M. Wang, H.F. Zhang, B.Z. Ding, and Z.Q. Hu: *Intermetallics*, 2002, vol. 10, p. 1283.
17. C.C. Hays, C.P. Kim, and W.L. Johnson: *Phys. Rev. Lett*., 2000, vol. 84, p. 2901.
18. G. He, W. Lösser, J. Eckert, and L. Schultz: *J. Mater. Res*., 2002, vol. 17, p. 3015.
19. G. He, W. Lösser, J. Eckert, and L. Schultz: *Nature Mater*., 2003, vol. 2, p. 33.
20. U. Kühn, J. Eckert, N. Mattern, and L. Schultz: *Appl. Phys. Lett*., 2002, vol. 80, p. 2478.
21. K.M. Flores and R.H. Dauskardt: *J. Mater. Res*., 1999, vol. 14, p. 638.
22. K. Fujita, A. Inoue, and T. Zhang: *Scripta Mater*., 2001, vol. 44, p. 1629.
23. C.J. Gilbert, R.O. Ritchie, and W.L. Johnson: *Appl. Phys. Lett*., 1997, vol. 71, p. 476.
24. C.J. Gilbert, V. Schroeder, and R.O. Ritchie: *Metall. Mater. Trans. A*, 1999, vol. A30, pp. 1739-53.
25. J.J. Lewandowski and P. Lowhaphandu: *Phil. Mag*., 2002, vol. 82, p. 3427.
26. V. Schroeder, C.J. Gilbert, and R.O. Ritchie: *Mater. Sci. Eng*., 2001, vol. A317, p. 145.
27. A. Tatschl, C.J. Gilbert, V. Schroeder, R. Pippan, and R.O. Ritchie: *J. Mater. Res*., 2000, vol. 15, p. 898.
28. J.A. Verduzco, R.J. Hand, and H.A. Davies: *Int. J. Fatigue*, 2002, vol. 24, p. 1089.
29. Y. Yokoyama, N. Nishiyama, K. Fukaura, and H. Sunada: *Mater. Trans., JIM*, 2000, vol. 41, p. 675.
30. Q.S. Zhang, S.D. Wu, S. D., H.F. Zhang, B.Z. Ding, and Z.Q. Hu: *Acta Metall. Sinica*, 2002, vol. 38, p. 265.
31. U. Essmann, U. Gösele, and H. Mughrabi: *Phil. Mag*., 1981, vol. 44, p. 405.
32. A. Hunsche and P. Neumann: *Acta Metall*., 1986, vol. 34, p. 207.
33. M. Saletore and R. Taggart: *Mater. Sci. Eng*., 1978, vol. 36, p. 259.
34. Z.F. Zhang, Z.G. Wang, and Z.M. Sun: *Acta Mater*., 2001, vol. 48, p. 2875.
35. H. Mughrabi, F. Ackermann, and K. Herz: *ASTM STP*, 1981, vol. 81, p. 5.
36. Z.F. Zhang and Z.G. Wang: *Acta Mater*., 2003, vol. 51, p. 347.
37. C.T. Liu, L. Heatherly, D.S. Easton, C.A. Carmichael, J.H. Schneibel, C.H. Chen, J.L. Wright, M.H. Yoo, J.A. Horton, and A. Inoue: *Metall. Mater. Trans. A*, 1998, vol. 29A, pp. 1811-20.
38. G. He, J. Lu, Z. Bian, D.J. Chen, G.L. Chen, G.H. Tu, and G.J. Chen: *Mater. Trans*., 2001, vol. 42, p. 356.
39. Z.F. Zhang, J. Eckert, and L. Schultz: *Acta Mater*., 2003, vol. 51, p. 1167.
40. Z.F. Zhang, G. He, J. Eckert, and L.Schultz: *Phys. Rev. Lett*., 2003, vol. 91, p. 04550501.
41. L.A. Davis and S. Kavesh: *J. Mater. Sci*., 1975, vol. 10, p. 453.
42. A. Inoue, W. Zhang, T. Zhang, and K. Kurosaka: *Acta Mater*., 2001, vol. 49, p. 2645.
43. P. Lowhaphandu, S.L. Montgomery, and J.J. Lewandowski: *Scripta Mater*., 1999, vol. 41, p. 19.
44. Z.F. Zhang J. Eckert, and L. Schultz: *J. Mater. Res*., 2003, vol. 18, p. 456.
45. S. Suresh: *Fatigue of Materials*, 2nd ed., Cambridge Press, Cambridge, United Kingdom, 1998.
46. W.J. Wright, R. Saha, and W.D. Nix: *Mater. Trans*., 2001, vol. 42, p. 642.
47. X.S. Xiao S.S. Fang, L. Xia, W.H. Li, Q. Hua, and Y.D. Dong: *J. Alloy Compounds*, 2003, vol. 351, p. 324.
48. A.T. Alpas, L. Edwards, and C.N. Neid: *Metall. Trans. A*, 1989, vol. 20A, pp. 1395-1409.
49. V. Bengus, P. Diko, K. Csach, J. Miskuf, V. Ocelik, E.B. Korolkova, E.D. Tabachnikova, and P. Duhaj: *J. Mater. Sci*., 1990, vol. 25, p. 1598.
50. L.A. Davis and Y.T. Yeow: *J. Mater. Sci*., 1980, vol. 15, p. 230.
51. A. Inoue, H.M. Kimura, and T. Zhang: *Mater. Sci. Eng*., 2000, vols. A294–A296, p. 727.
52. J. Megusar, A.S. Argon, and N.J. Grant: *Mater. Sci. Eng*., 1979, vol. 38, p. 63.
53. T. Mukai, T.G. Nieh, Y. Kawamura, A. Inoue, and K. Higashi: *Scripta Mater*., 2002, vol. 46, p. 43.
54. N.I. Noskova, N.F. Vildanova, Y.I. Filippov, and A.P. Potapov: *Phys. Status Solidi A*, 1985, vol. 87, p. 549.
55. S. Takayama: *Scripta Metall*., 1979, vol. 13, p. 463.